**Witold Paleczek**
Dr inż.
Politechnika Częstochowska
Wydział Budownictwa
witold.paleczek@pcz.pl

# Hydrodynamic impact in an attempt to assess the possibility of analyzing the causes of damage to asphalt concrete pavement

**Abstract**: The phenomenon of hydrodynamic impact was presented as an attempt to assess the possibility of including this phenomenon as one of the main caused leading to the formation of damage to the asphalt concrete pavement. This phenomenon occurs regardless of the season. Pavement damage caused by the freezing of water solutions in the mesh cracks and line cracks is widely known and, as well as swelling ice in clay soil, are among the main caused of pavement damage. It was justified that the hydrodynamic impact caused by the wheels of the front a then the rear axle of the vehicle with elastic tires causes the formation of wave phenomena that may lead to exceeding the material effort. Exceeding the permissible stresses in the formant range of the resonant frequency may lead to the loss of cohesion and load capacity of this material.)

**Keywords**: Hydrodynamic impact; Damage to road surfaces; FFT analysis; Material effort

## Introduction

The damage to road surfaces is caused by several factors, among which the most significant are:

- **Traffic load:** Effects of cyclic loads, localized overloads of the pavement, abrasion, rutting, cracking of the wearing course leading to the formation of longitudinal and alligator cracks, and ultimately the emergence of potholes and road failures [2, 23, 25, 26];
- **Hydrological changes:** Effects of erosion caused by water runoff and improper drainage from the road base due to water stagnation, as well as frost heave formation in the layers beneath the pavement during freezing periods;
- **Thermal changes:** Effects of local thermal gradient formation, consequences of water solution freezing in pavement voids due to temperatures dropping below the freezing point;
- **Subgrade deformations:** Due to material leaching from the road base, landslides, or subsurface deformations in areas classified as mining regions;
- **Chemical erosion:** Effects of salt crystallization from water solutions in cracks [7, 8, 9, 10, 14, 21, 22, 30].

An analysis of the locations of road surface damage, not only those made of asphalt concrete, indicates that areas where water accumulates and where vehicles subsequently travel are more susceptible to mechanical damage. Such damage is attributed to the impact of low temperatures below the freezing point of the solution. It is well known that liquid volume increases upon freezing, which leads to increased tensile stress and, ultimately, local material cohesion loss, creating pavement voids.

Figure **1** presents asphalt pavement damage caused by improper drainage of rainwater. Figure **2** illustrates water condensation during winter from cracks in the fractured asphalt pavement, beneath which frost heaves have formed. Figure **3** shows potholes and asphalt pavement voids with visible water accumulation, also highlighting the destructive mechanism of water solution retention by geotextiles (the recorded damages occurred during winter).

Figure **4** depicts a damaged section of an asphalt concrete road lane with visible water solution stagnation in pavement voids that reach down to the base layer.





**1.** Grid, block cracks and cavites – an example of damage to an asphalt pavement due to the lack of proper drainage of rainwater, followed by frost.

**2.** Grid, block and line cracks – damage to the asphalt surface consisting in its cracking as a result of the formation of icy swelling in the base of road; water from melted ice from the foundation, under the influence of gravity and external load, the water flows to the upper road surface of the surface heated by solar radiation.
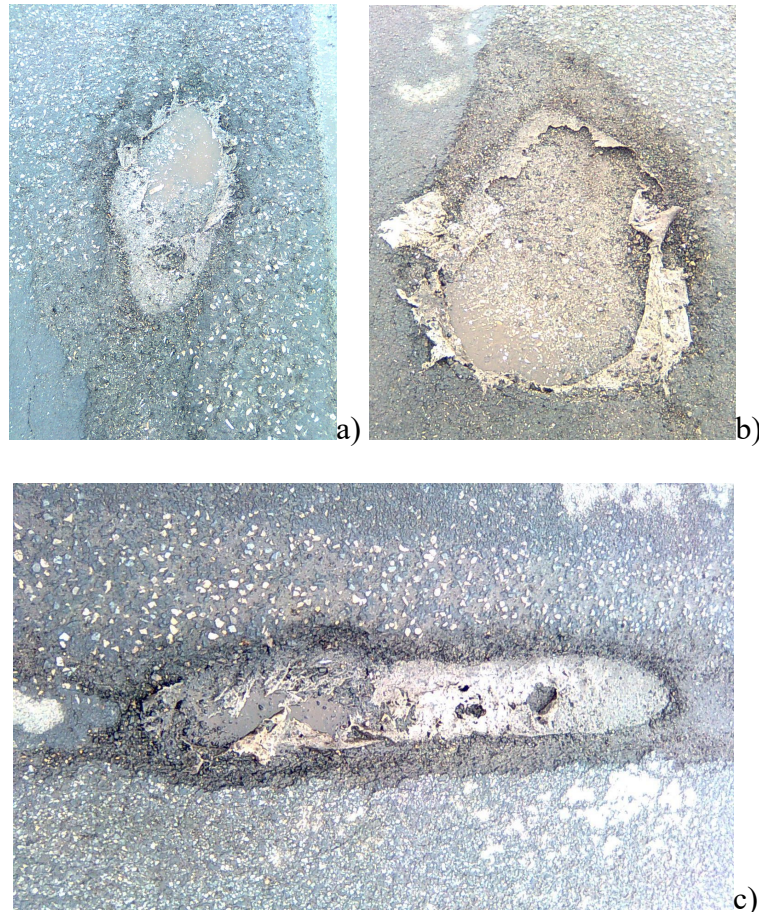
**3.** Potholes/cavites/bumps – examples of extensive superficial damage to the asphalt concrete wearing course: wearing course separated by a fabric from the binder course: a) elliptica-circular pit damage with considerable amount of stagnant water; b) a circular pit hole with stagnant water in the binder course; c) deep damage to the surface of an elliptical-longitudinal shape with a visible fragment of the ice lens (on the left) – deep erosion of the binder layer under the damaged textile layer is also visible.
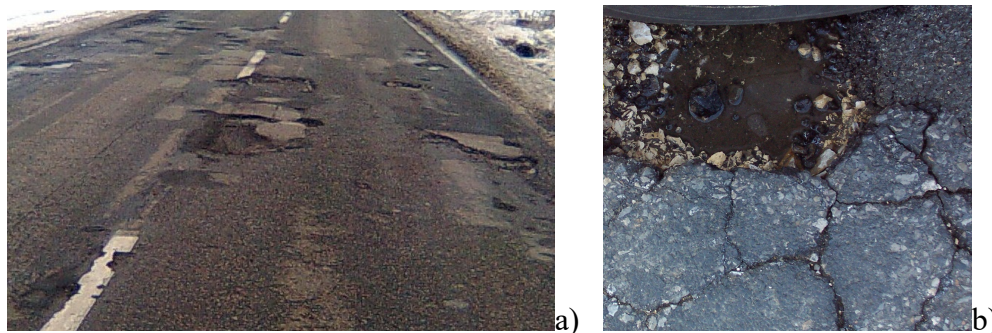


**4.** Bumps:  a) A fragment of the road surface with significant losses in the wearing course made of asphalt concrete, in the binding layer and in the foundation; b) vehicle wheel in a deep loss of the surface road layer up to the foundation, with water stagnation visible.

## Aqueous Solutions in Winter

During the winter season, road surfaces are treated with salt mixtures designed to lower the freezing temperature of water solutions. Various salts and their mixtures are used for this purpose [8, 14, 15, 19, 20, 21].

Analyses of the freezing process of certain aqueous salt solutions have enabled the development of proposed empirical formulas, which may prove useful in estimating the

freezing temperaturę $t$ [°C], depending on the percentage content of a given salt, expressed in $p$ [%] [17].

- For NaCl, the obtained relationship is given by equation (1).
- For MgCl$_2$, the corresponding formula is equation (2).
- For CaCl$_2$, the relationship is described by equation (3).

The summary of these relationships is presented in the collective graph in Figure **5**. The visualization of empirical formulas (1) ÷ (3) highlights that there exist aqueous solutions capable of remaining in a liquid state even at temperatures as low as -40°C.

$$^{NaCl}t(p) = \begin{cases} -0{,}222 \cdot p^{1{,}46} & dla \quad 0 < p < 21{,}2\% \\ (0{,}0001 \cdot e^{0{,}48 \cdot p}) - 22 & dla \quad p \geq 21{,}2\% \end{cases} \tag{1}$$

$$^{MgCl_2}t(p) = \begin{cases} -0{,}25 \cdot p^{1{,}44} & dla \quad 0 < p < 27{,}2\% \\ 0{,}0027 \cdot p^3 - 0{,}328 \cdot p^2 + 13{,}75 \cdot p - 215 & dla \quad p \geq 27{,}2\% \end{cases} \tag{2}$$

$$^{CaCl_2}t(p) = \begin{cases} -0{,}06 \cdot p^{1{,}79} & dla \quad 0 < p < 44{,}2\% \\ (0{,}25637 \cdot p \cdot e^{4{,}5-0{,}014 \cdot p}) - 602 & dla \quad p \geq 44{,}2\% \end{cases} \tag{3}$$
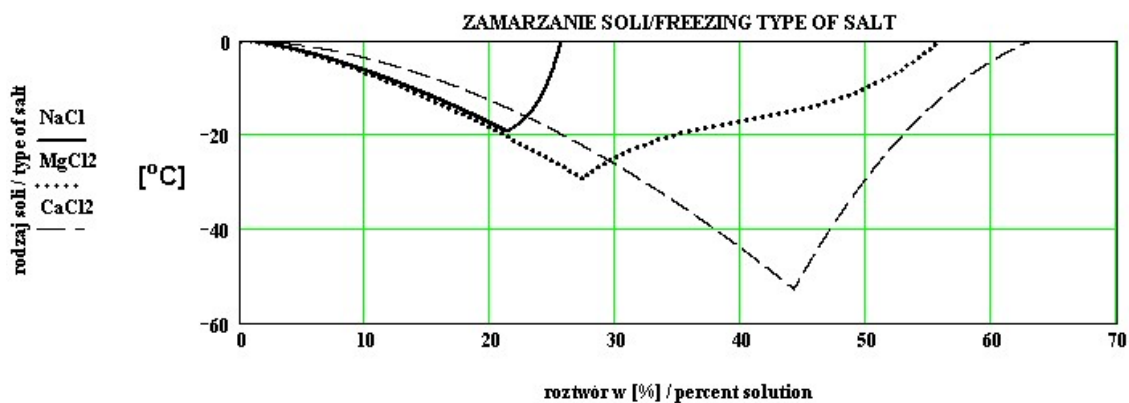


**5.** Graphs of freezing of aqueous (percentage) solutions of salts NaCl – marking with a solid line; MgCl$_2$ – marking with a dotted line; CaCl$_2$ – marking with a dashed line. The area "inside the curve" is "solution"; the area to the right of the extreme point is "solution and salt"; the area below the extreme temperature is "ice and salt side by side"; the area from "0" to the point of extreme is "ice and solution".

**Hydraulic Impact vs. Hydrodynamic Impact**
In the literature, two distinct types of dynamic fluid interactions with surrounding structures are generally recognized.

- One of them is the phenomenon known as hydraulic impact, which occurs in pipelines and involves the sudden stoppage of a fluid stream moving at high velocity within an installation. This phenomenon, however, is not the subject of this study.
- In contrast, hydrodynamic impact involves significant compression of a fluid within a given volume, followed by expansion, which causes an impact load on the surrounding structure due to the mass of the fluid (e.g., high-pressure fluids used in machining processes) [5, 6, 12, 27, 28, 29].

In the case of a pavement void filled with liquid, the elastic tire of a wheel passing over the void leads to fluid compression—analogous to the "piston compression in a cylinder" phenomenon. Figure **6** presents the simplest schematic representation of the load from a single wheel, which is used in subsequent simplified model calculations.
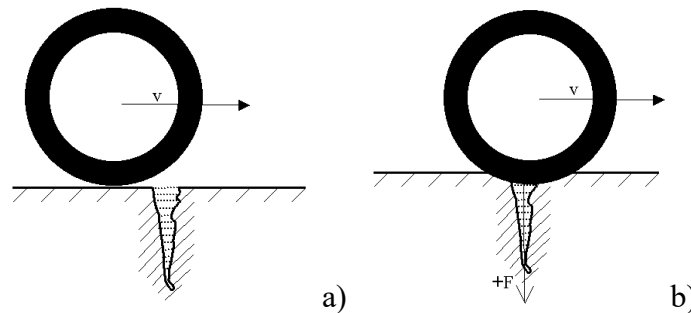
**6.** Illustration showing a diagram of a single „water hammer", which can cause extensive mechanical damage to a cracked road surface: a) a wheel of a vehicle traveling at speed „v" in front of a liquid-filled gap; b) the entry of a whell with elastic tires on a gap filled with liquid – the pressure of the compressed liquid causes stresses acting as in the case of "water hammer".

**Finite Element Method (FEM) Model Calculations**

Using the capabilities of Finite Element Method (FEM) modeling, an analysis was conducted on the deformation of an isotropic material subjected to loads that could be analogous to the stress exerted on a pavement crack by a freezing aqueous solution [4, 16, 31].

The liquid pressure was modeled as a continuous load applied to the surface and mesh nodes on the inner side of the simulated pavement void. The adopted model provides an approximate analogy to the phenomenon of pressure increase due to solution freezing.

- Figure **7a** presents a section of the FEM mesh, supplemented with a load distribution schematic.
- Figure **7b** illustrates the theoretical continuous deformation of the assumed model under the applied load conditions.
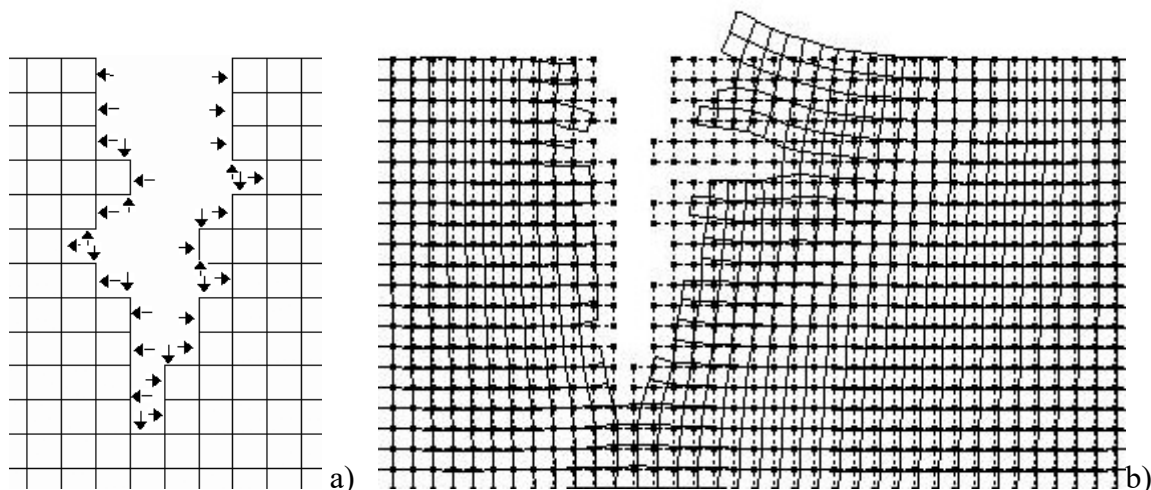


**7.** a) Scheme of the uniform distribution of forces acting on the crack walls at a fixed liquid pressure (fragment of the FEM model mesh); b) – result of FEM model deformation calculations – exemplary deformation of an isotropic material with a given load scheme.

In the next FEM model, an analysis was conducted to evaluate the material stress under a steady-state condition. The model was designed to represent voids in the material, simulating pavement damage.

- It was assumed that the walls of the void located on the left side of the model are subjected to linear loading.
- In contrast, the walls of the second void remain unloaded.

The material was considered isotropic but asymmetrical in stress response. The material stress was determined using the generalized Mohr's hypothesis, which in a plane stress state is expressed by the following equation (4):

$$\sigma_{11}^2 + \sigma_{22}^2 + 2 \cdot \sigma_{12}^2 - 2 \cdot v \cdot \left(\sigma_{11} \cdot \sigma_{22} - \sigma_{12}^2\right) - \left(\overline{\sigma} + \underline{\sigma}\right) \cdot \left(\sigma_{11} + \sigma_{22}\right) + \overline{\sigma} \cdot \underline{\sigma} = \Xi \qquad (4)$$

In which:

$\sigma_{11}, \sigma_{22}, \sigma_{12}$ – normal and shear stresses respectively,

$v$ – Poisson's number,

$\overline{\sigma}, \underline{\sigma}$ – allowable compressive and tensile stresses respectively,

$\Xi$ – material effort according to the given effort hypothesis, [13, 18, 24].

In areas where the greatest material stress occurs, damage can be expected in the form of loss of continuity within the material.

- Figure **8** presents the calculated results, including sections of the deformed mesh structure and a stress distribution map from the FEM model.
- On the stress map (Figure **8b**), the lighter shades indicate regions of highest stress concentration.
  From the calculation results, it can be inferred that:
1. A void filled with pressurized liquid may deepen further due to stress.
2. The material section separating two voids is susceptible to detachment, potentially leading to progressive structural degradation.



a)



b)
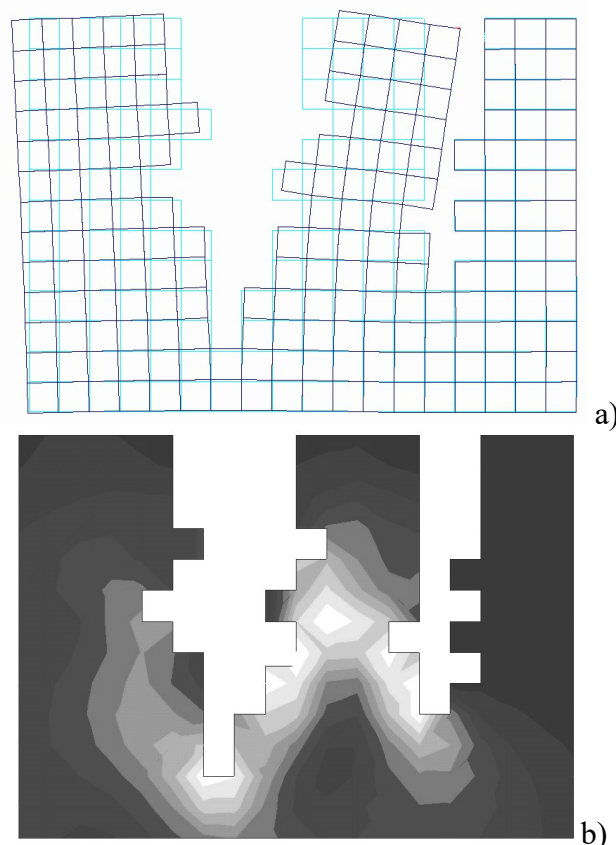
**8.** FEM model of material effort in a plane stress state with given geometry and material constants of an isotropic material; a) a larger defect area in the analyzed vertical section corresponds to a „crack filled with pressurized liquid", while a smaller defect area corresponds to the adjacent "empty gap", unloaded; b) isoline map of the effort of isotropic material: a lighter shade indicates the effort of the material at which a loss of continuity may occur.

**Simplified Computational Model of Tire Impact on a Liquid-Filled Crack**
For this analysis, a "hydrodynamic impact" model was considered, formulated using a second-order matrix differential equation of the form, [5, 6, 11, 16, 24]:

$$\mathbf{m\ddot{u} + c\dot{u} + ku = F}(t) \tag{5}$$

In which:
**m** - Mass matrix (Inertia matrix),
**u** - Nodal displacement matrix (Generalized coordinate matrix)
**c** - Damping matrix,
**k** - Stiffness matrix,
**F**(t) - Dynamic excitation matrix (Load matrix)

In the numerical model, an analogy to a multilayer pavement model was adopted with given values contained in the inertia, stiffness, and damping matrices. In the computational test, it was assumed that the analysis simultaneously covers seven layers: the first layer in the model, marked on the charts with the variable "w7," is excited by impact impulses spaced apart in time by a value resulting from equation (6). This equation includes two impulses, so an analogy to a two-axle vehicle (function F(t)) was assumed. In the case of a five-axle vehicle, the impact impulses were determined as in equation (7) – (function FC)(t)):

$$F(t) = a_0 \cdot e^{-b_0 \cdot (t-t_0)^2} + a_1 \cdot e^{-b_1 \cdot (t-(t_0+t_{12}))^2} \tag{6}$$

$$FC(t) = c_0 \cdot e^{-d_0 \cdot (t-t_0)^2} + c_1 \cdot e^{-d_1 \cdot (t-(t_0+tc_{12}))^2} + c_2 \cdot e^{-d_2 \cdot (t-(t_0+tc_{12}+tc_{23}))^2} +$$
$$+ c_3 \cdot e^{-d_3 \cdot (t-(t_0+tc_{12}+tc_{23}+tc_{34}))^2} + c_4 \cdot e^{-d_4 \cdot (t-(t_0+tc_{12}+tc_{23}+tc_{34}+tc_{45}))^2} \tag{7}$$

With the markings:

$$a = \begin{bmatrix} 1 \\ 1 \end{bmatrix}, \; b = \begin{bmatrix} 13 \cdot 10^3 \\ 13 \cdot 10^3 \end{bmatrix}, \; c = \begin{bmatrix} 4 \\ 4 \\ 4 \\ 4 \end{bmatrix}, \; d = \begin{bmatrix} b_0 \\ b_1 \\ b_2 \\ b_3 \end{bmatrix}, \; t_0 = 0.1 \; [s]$$

$$t_{12} = \frac{2.7 \; [m]}{v \left[\frac{m}{s}\right]}, \; tc_{12} = \frac{3.7 \; [m]}{v \left[\frac{m}{s}\right]}, \; tc_{23} = \frac{7.16 \; [m]}{v \left[\frac{m}{s}\right]}, \; tc_{34} = \frac{1.21 \; [m]}{v \left[\frac{m}{s}\right]}, \; tc_{45} = \frac{1.21 \; [m]}{v \left[\frac{m}{s}\right]}$$

In which:
$a_i, b_i, c_i, d_i$ – empirical values modeling the impact excitation in the time domain,

$t_0$ – distance on the time axis of the first shock excitation pulse from the origin of the coordinate system: assumed constant value in all computational tests $t_0 = 0.1 \; [s]$;

$t_{12}$ – the time needed to travel a distance equal to the distance between the axles of a two-axle vehicle, at a given travel speed $v$;

$tc_{12}, tc_{23}, tc_{34}, tc_{45}$ – names of variables defining the time needed to travel a distance equal to the distances of adjacent axles of a five-axle vehicle at a given speed $v$.

In the calculations, it was assumed that each impact excitation impulse is modeled by a curve similar in shape to a normal distribution. The range of travel speeds was analyzed within the interval from 15 [km/h] to 100 [km/h]. The solutions to equation (5) under the given impact excitation functions defined by equations (6) and (7) were obtained using the

Runge-Kutta method. This method was implemented with an algorithm that generates solutions at equal division steps within the integration interval, allowing direct execution of further calculations using the FFT without requiring additional data quantization [16].

Figure (9) presents an example of the forcing function (in the time domain), while Figure (10) shows a cumulative plot of the solution to equation (5). Since the formulated problem requires reasoning in the frequency domain during computations, the Fast Fourier Transform (FFT) algorithm defined by equation (8) was used for this purpose. The variable name "w7" indicates that the calculations pertain to the first analyzed layer in the adopted seven-layer model, while "w1" refers to the last layer):

$$\left|\Gamma 7_u\right| = \sqrt{\mathrm{Re}\left[FFT\left(w7_\xi\right)\right]^2 + \mathrm{Im}\left[FFT\left(w7_\xi\right)\right]^2} \tag{8}$$

The results obtained from equation (8) enable the analysis of frequency bands of the main formants (formant analysis). In this analysis, the spectral amplitude is determined by equation (9), while the spectral frequency is given by equation (10), [1, 3, 11, 15, 17]:

$$A7_u = \left(\left|\Gamma 7\right|_u\right)^2 \cdot \left(f_u\right)^2 \tag{9}$$

$$f_u = \frac{u \cdot \tau_2}{\tau_1} \tag{10}$$

With the markings:

$u = \tau_1 - 1$ – variable indexing the frequency relative to discretized time,

$t = \tau_0, \dfrac{\dfrac{\tau_1}{\tau_2} - \tau_0}{\tau_1 - 1} .. \dfrac{\tau_1}{\tau_2}$ – discretized time, adapted to FFT on a set of samples $2^n$, whose elements

are arranged in a vector $\tau = \begin{pmatrix} 0 \\ 2^n \\ f_s \end{pmatrix}$, at sampling rate $f_s$.

**Results of the Analysis of Dynamic Excitations in Time and Frequency Domains**

The calculations conducted in this study demonstrate an analogy to impact excitations generated by two vehicle models: a two-axle and a five-axle vehicle, both traveling individually at a given speed and unilaterally rolling their axle wheels over a single pavement crack filled with liquid.

For the two-axle vehicle model, an axle spacing of 2.7 [m] was assumed, corresponding approximately to the axle spacing found in many passenger car models. In the case of the five-axle vehicle model, a multi-unit vehicle was selected, consisting of a two-axle tractor unit with an axle spacing of 3.7 [m] and a three-axle trailer with axle spacings of +7.16 [m] + 1.21 [m] + 1.21 [m], resulting in a total extreme axle spacing of 13.28 [m].

It was assumed that the surroundings of the crack filled with liquid consist of seven layers. Each layer is characterized by material constants defined in equation (5). The impact excitations over time are proportional to the vehicle axle spacing and their test speeds, as specified in equations (6) and (7).

Figure **9** presents the time-domain excitation plot for the two-axle vehicle model at a test speed of 45 [km/h], while Figures **12** and **15** illustrate the same for the five-axle multi-unit vehicle. In the time-domain calculations, the distances between impact excitation pulses and the displacement plots of successive layers were analyzed (see Figures **10**, **13**, **16**).

In the frequency domain, amplitude values and the positions of individual formants at a given travel speed were examined (see Figures **11**, **14**, **17**). The maximum amplitude values

were used to create dependency plots of the main formants within the analyzed spectral frequency range, corresponding to the maximum amplitude values (see Figures **18**, **19**, **20**). In addition to formant analysis, the relevant FFT spectrum plots defined by the equation were extracted (8).
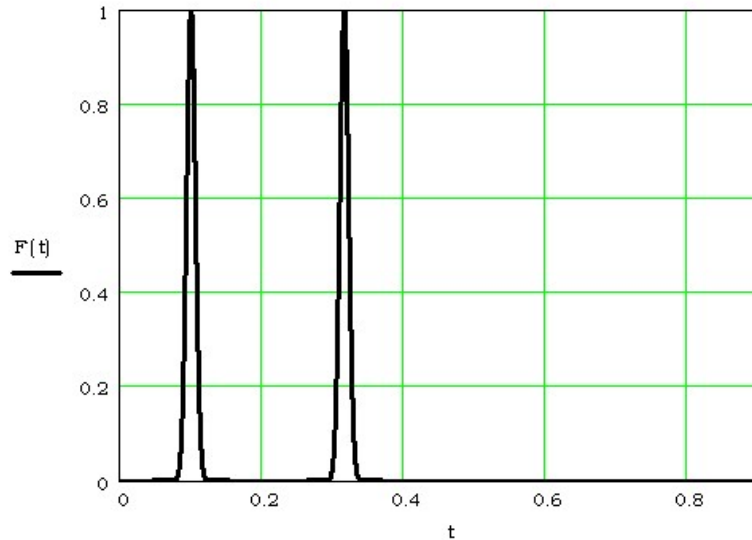


**9.** Graph of the excitation pulses of layer system in the model over time – two-axle vehicle, here: wheelbase 2,7 [m], movement at a speed of 45 [km/h].
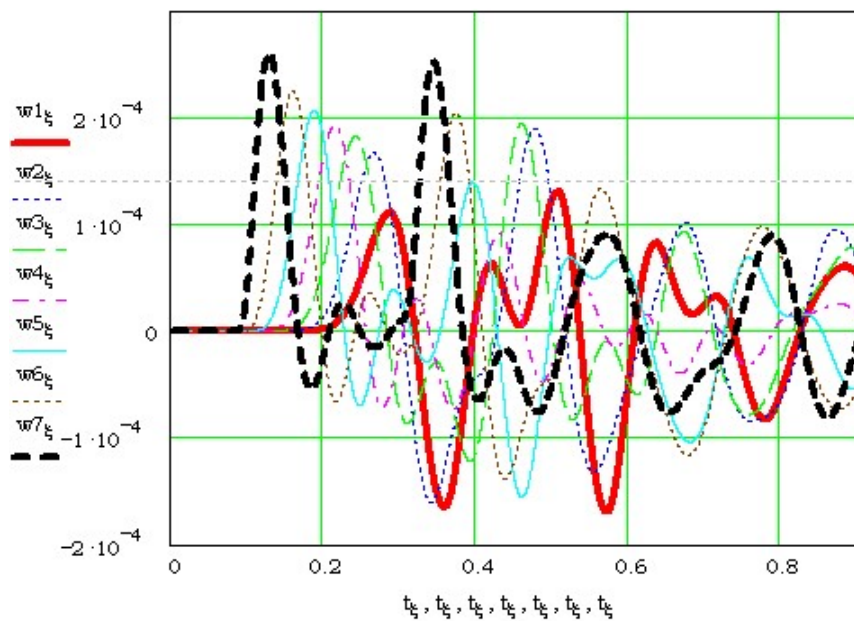


**10.** Summary chart of vertical displacements of seven layers of the pavement model analyzed in this time interval. Excitation (load) by passing a two-axle vehicle with a wheelbase of 2,7 [m], at a speed od 45 [km/h]. Markings: (w7) outer layer (first) marked with a bold dashed line; (w1) the outer (inner) layer in the model, marked with a thick solid line; (w2-w6) intermediate layers located between (w7) and (w1).
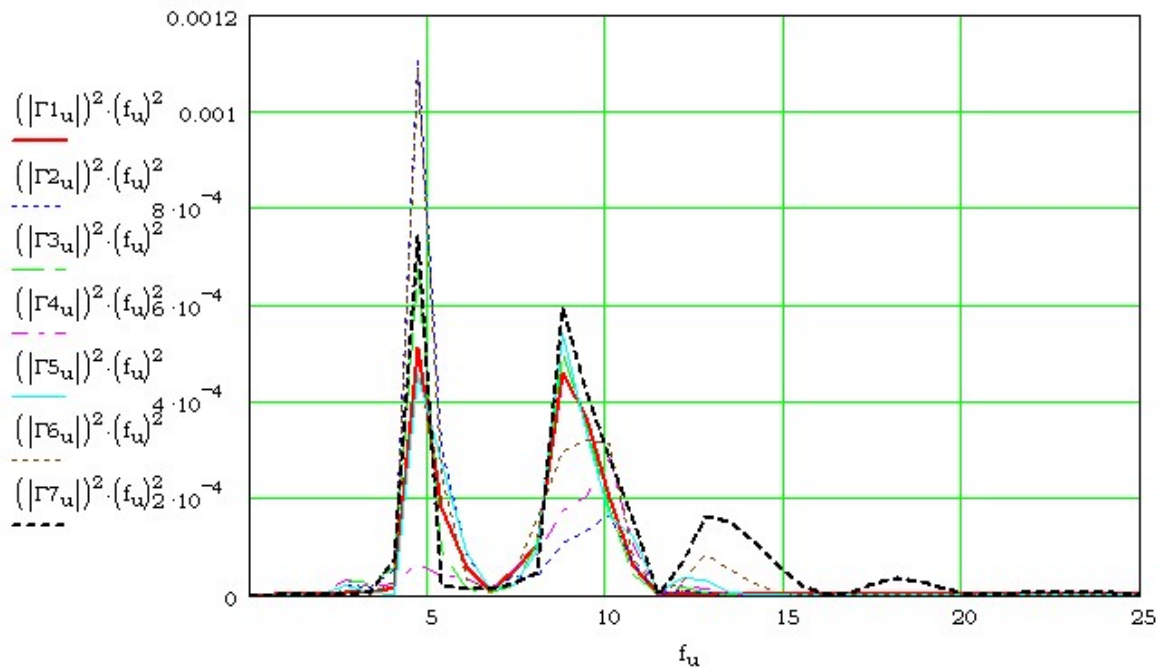
a)
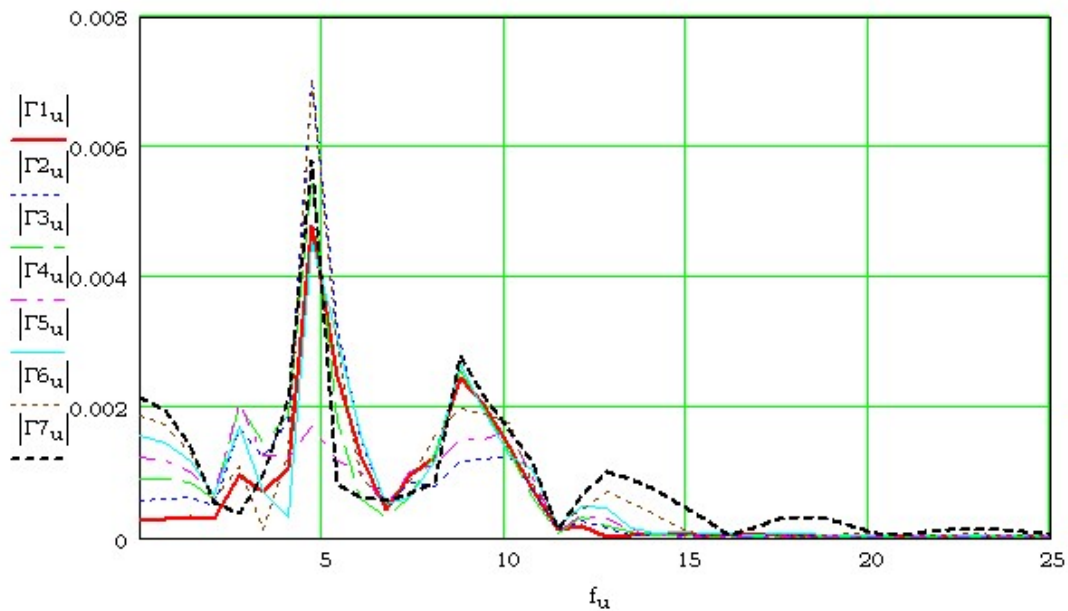


b)

**11.** a) Graph of main formant amplitude versus frequency, frequency in [Hz]. Markings: dashed bold line refers to the outer layer (w7); the solid line in bold refers to the inner, outer layer (w1); the remaining lines refer to the intermediate layers between (w7) and (w1); the example concerns a two-axle vehicle with an axle span of 2,7 [m] traveling at a speed of 45 [km/h]; b) spectra FFT – formula (8).
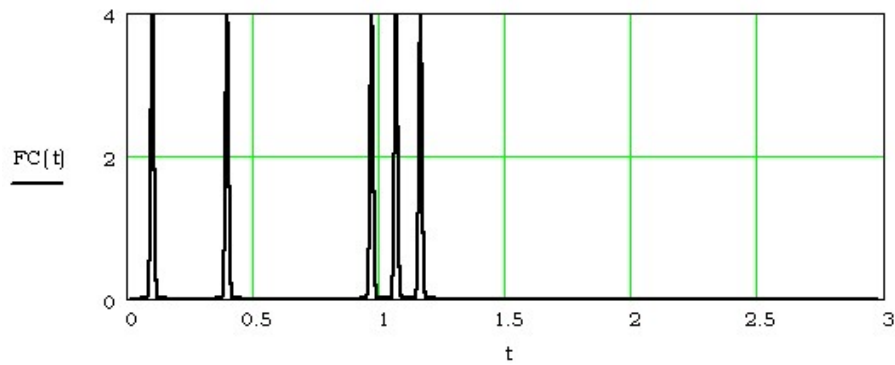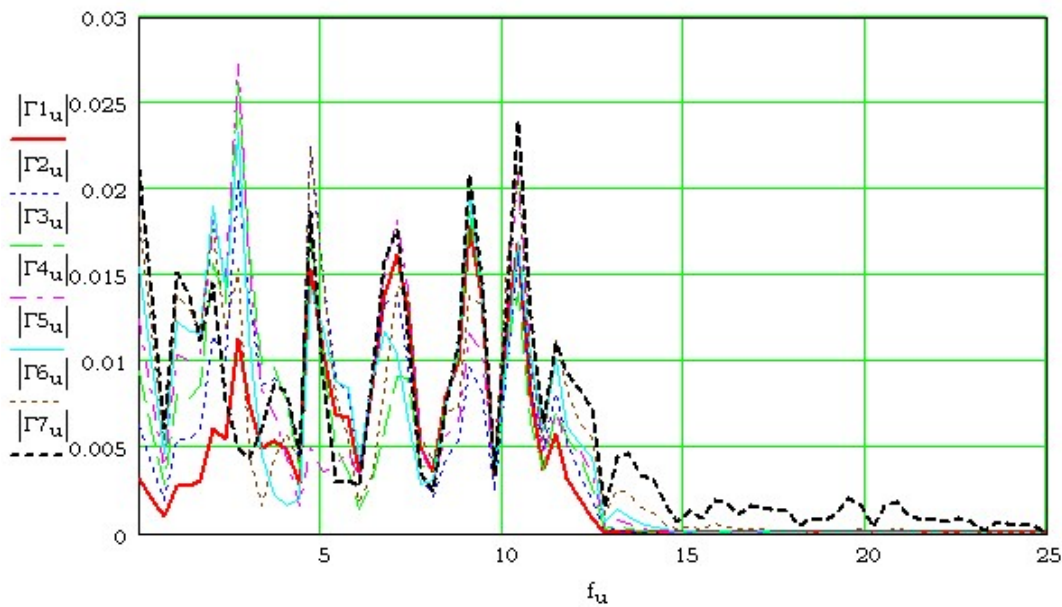
**12.** Plot of the impact excitation of the layer system in the model in the time domain, [s]; five-axle vehicle; here: wheelbase (two-axle truck tractor) 3,7 [m] + (three-axle semi-trailer) +7,16 [m] +1,21 [m] +1,21 [m]; traveling at a speed of 45 [km/h].
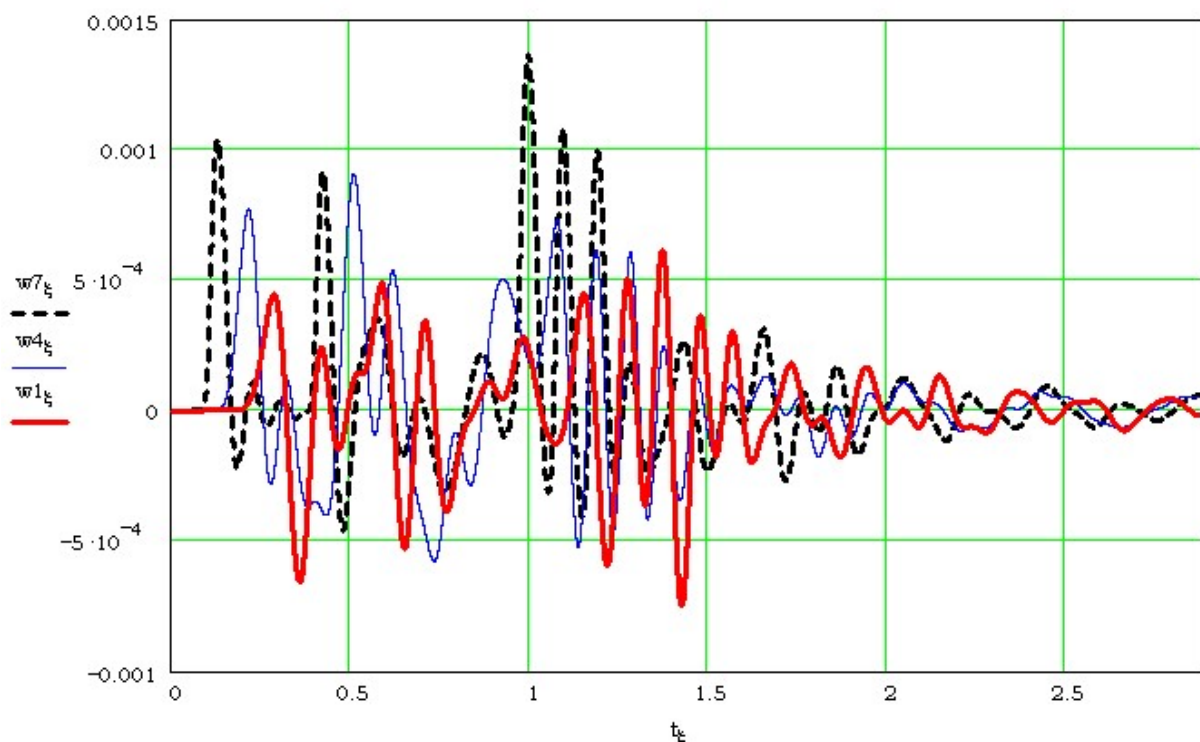


**13.** Summary diagram of layer displacements in the time [s] domain under dynamic excitation, the illustration of which is shown in Fig. 12. Symbols: (w7) – first layer – dashed, bold line; (w4) – intermediate layer – continuous, thin line; (w1) – last layer in the model – solid, bold line; five-axle vehicle, movement speed 45 [km/h].
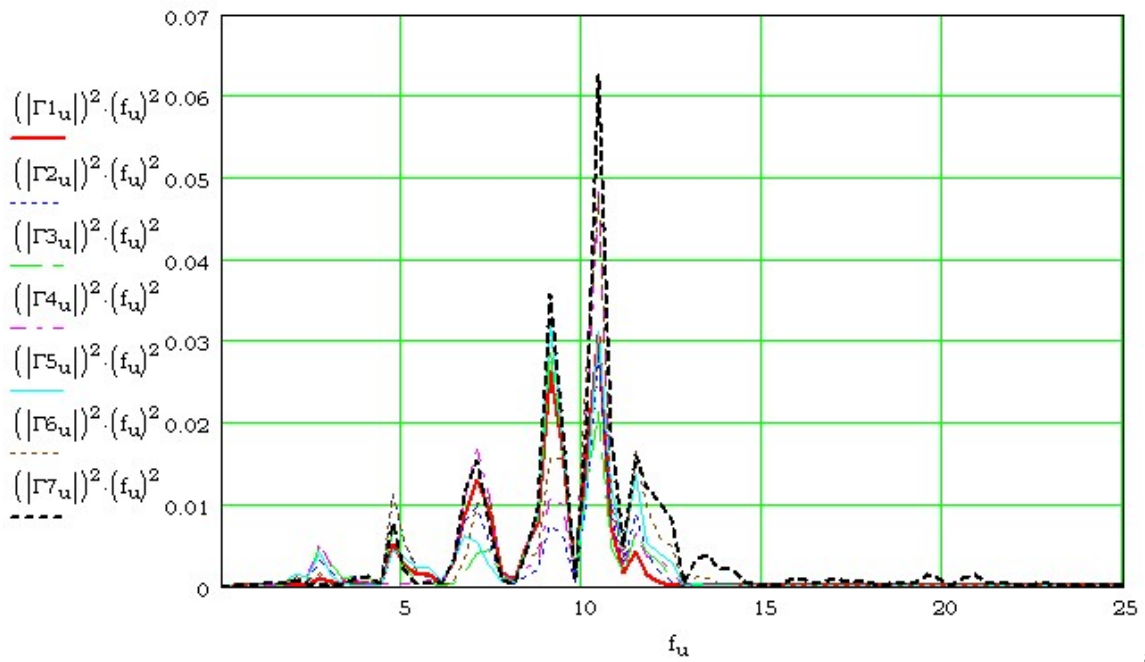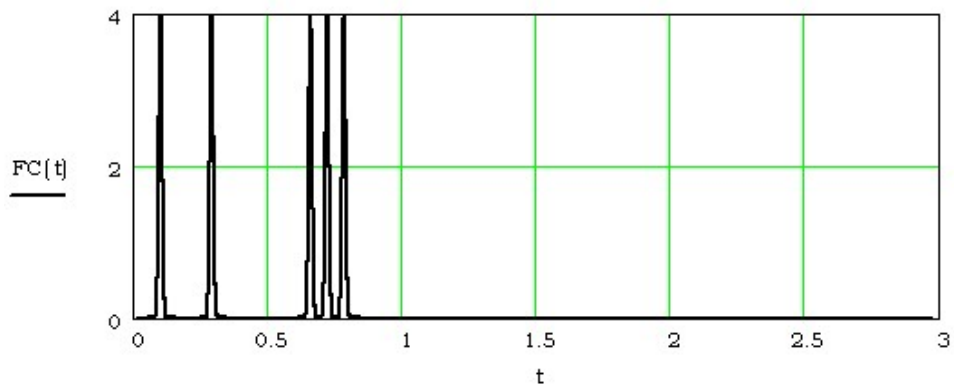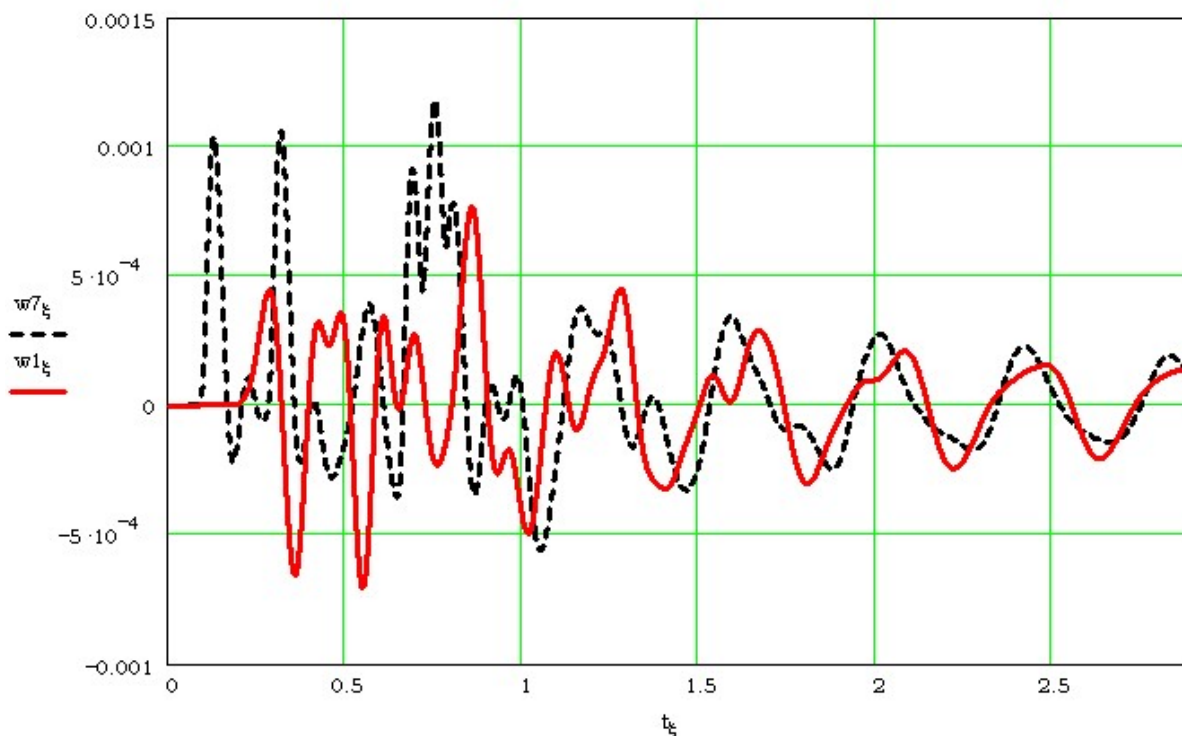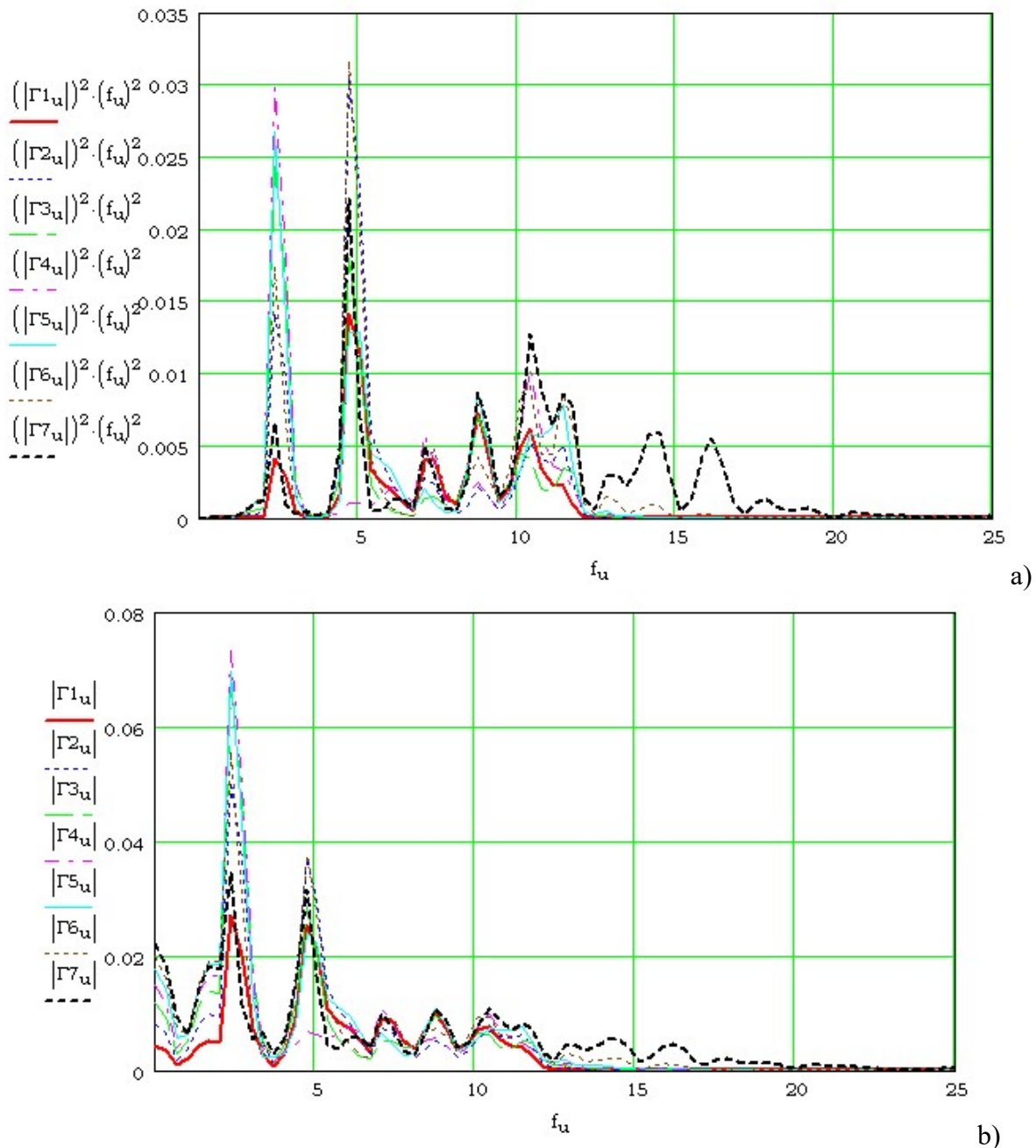
**14**. a) Summary list of the main excitation formants of the model layers from the spatial analysis in the frequency domain [Hz]. Illustration of shock excitations in Figure 12; five-axle vehicle, traveling at a speed of 45 [km/h]. Symbols: ($\Gamma7$) – first layer in the model – dashed, bold line; ($\Gamma6$) do ($\Gamma2$) – intermediate layers – presentation with thin lines; ($\Gamma1$) – last layer – solid, bold line; b) spectra FFT – formula (8).

**15.** Plot of the impact excitation of the layer system in the model in the time domain, [s]; five-axle vehicle; here: wheelbase (two-axle truck tractor) 3,7 [m] + (three-axle semi-trailer) +7,16 [m] +1,21 [m] +1,21 [m]; traveling at a speed of 70 [km/h].



**16.** Summary diagram of layer displacements in the time [s] domain under dynamic excitation, the illustration of which is shown in Fig. 15. Symbols: (w7) – first layer – dashed, bold line; (w1) – last layer in the model – solid, bold line.

**17.** a) Summary list of the main excitation formants of the model layers from the spatial analysis in the frequency domain [Hz]. Illustration of shock excitations in Figure 15; five-axle vehicle, traveling at a speed of 70 [km/h]. Symbols: ($\Gamma7$) – first layer in the model – dashed, bold line; ($\Gamma6$) do ($\Gamma2$) – intermediate layers – presentation with thin lines; ($\Gamma1$) – last layer – solid, bold line; b) spectra FFT – formula (8).
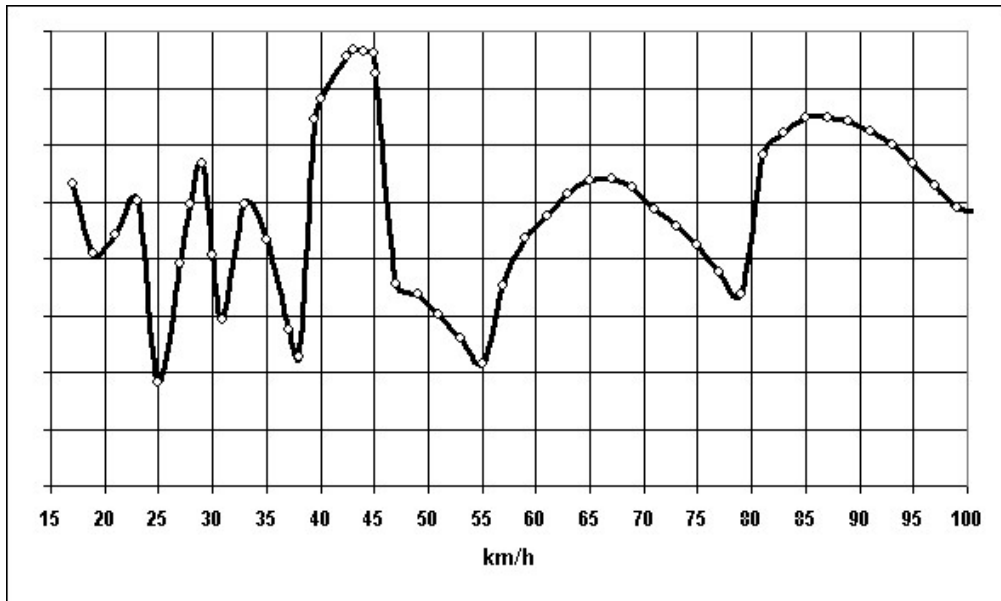
**18.** Graph of the dependence of the main formants in the range of the analysed spectral frequencies with the maximum value of the amplitude: dependence on the speed of the two-axle vehicle (average formants values from the outer, middle and inner extreme layer in the pavement model); there is a speed range at which the load transferred to the pavement and ground has the highest energy; here: range of speed from 39 to 45 [km/h].
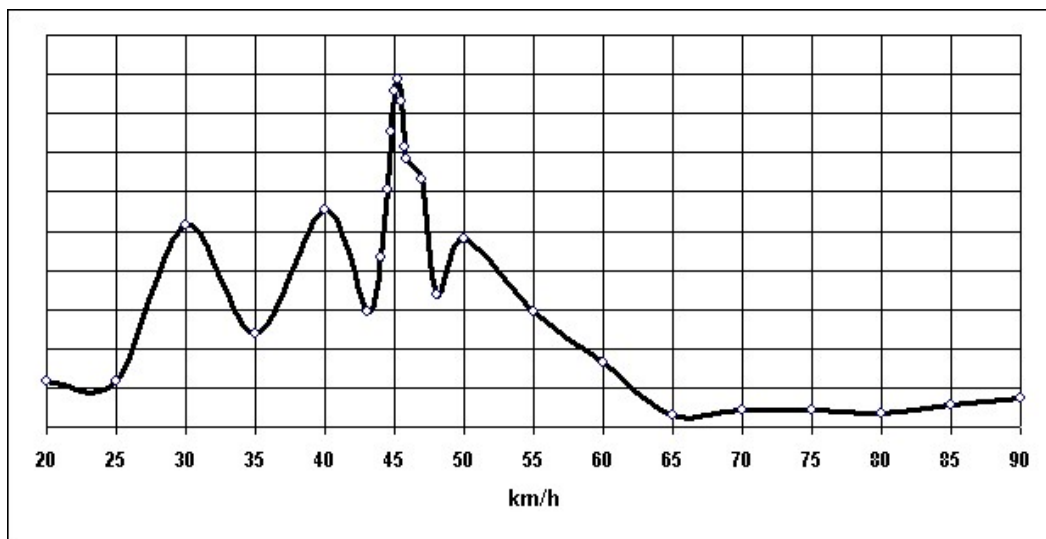


**19.** Graph of the dependence of the main formants in the range of the analysed spectral frequencies with the maximum value of the amplitude: dependence on the speed of the five-axle vehicle (average formants values from the outer, middle and inner extreme layer in the pavement model); there is a speed range at which the load transferred to the pavement and ground has the highest energy; here: range of speed from 44 to 46 [km/h].
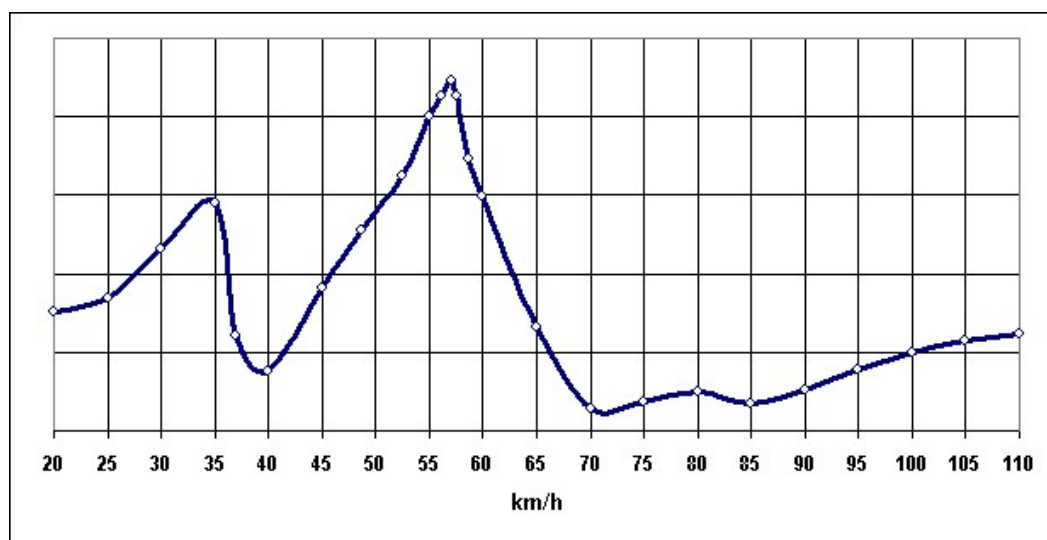
**20.** Graph of the dependence of the main formants in the range of the analysed spectral frequencies with the maximum value of the amplitude: dependence on the speed of the five-axle vehicle (average formants values from the outer, middle and inner extreme layer in the pavement model); there is a speed range at which the load transferred to the pavement and ground has the highest energy; here: range of speed from 53 to 60 [km/h]; elasticity and damping in the multi-layer model increased by 1/5.

**Conclusions**

The analysis of the hydrodynamic impact phenomenon was simplified here by reducing it to solving equation (5) under impact excitations defined by equations (6) and (7). Subsequently, a spectral FFT analysis was performed on the solutions obtained from the differential equation in the time domain, along with an analysis of the frequency of occurrence of the main formant.

The calculations carried out on multilayer numerical models confirmed the assumption that there is a "dangerous" velocity range for various material constants defined by the elasticity and damping of the pavement material. Under a given impact excitation, this velocity range corresponds to the maximum energy transfer from the vehicle's wheels (here: the frequency of occurrence of the main formant at a given travel speed).

It can be assumed that if the main formant coincides with the resonant frequency of the material, its damage occurs in the shortest possible time. Hydrodynamic impact may significantly affect the deterioration of asphalt concrete pavements, and conclusions from deterministic models should be supplemented and verified through research on real-world structures.

**Source materials**

[1]   Ciesielski R., Maciąg E., Drgania drogowe i ich wpływ na budynki.WKiŁ, Warszawa 1990
[2]   Ciesielski R., Maciąg E., Spektra odpowiedzi drgań wywołanych ruchem drogowym. Mechanika nr 12, Wydawnictwa Krakowskiego Oddziału PAN, Kraków 1986, s. 27-46
[3]   Ciesielski R., Ocena szkodliwości wpływów dynamicznych w budownictwie. Arkady, Warszawa 1973
[4]   Grajek K., ABC Płyta.Tarcza.Rama. Pro-Soft, Gliwice 2000
[5]   Gryboś R., Drgania konstrukcji wzbudzone przepływem. Wydawnictwo Politechniki Śląskiej, Gliwice 2005
[6]   Gryboś R., Mechanika płynów. Wydawnictwo Politechniki Śląskiej, Gliwice 1991
[7]   Iwański M., Mazurek G., Wodo- i mrozoodporność betonu asfaltowego produkowanego w technologii ciepłej = Water und frost resistance of asphalt concrete produced in the

warm technology. 10th International Conference Modern Building Materials, Structures and Techniques, Wilno 2010, s.200-206

[8] Jaskuła P., Judycki J., Wpływ starzenia i oddziaływania wody i mrozu na zmianę właściwości mieszanek mineralno-asfaltowych. VIII Konferencja Naukowa Komitetu Inżynierii Lądowej i Wodnej PAN i Komitetu Nauki PZITB, Krynica 2002, s.221-233

[9] Judycki J., Budowa i kalibracja modeli spękań zmęczeniowych warstw asfaltowych nawierzchni drogowych w mechaniczno-empirycznej metodzie AASHITO 2004. Drogi i Mosty, nr 4/2011, s. 31-53

[10] Kalabińska M., Gaweł I., Piłat J., Asfalty drogowe. WKiŁ, Warszawa 2001

[11] Kucharski T., System pomiaru drgań mechanicznych. WNT, Warszawa 2002

[12] Landau L., Lifszyc E., Hydrodynamika. PWN, Warszawa 1994

[13] Marks W., Optymalizacja według kryteriów wytężeniowych. Kryteria i metody optymalizacji konstrukcji. IPPT PAN, PWN, Warszawa 1977

[14] Mazurek Grzegorz, Wpływ starzenia na właściwości betonu asfaltowego z asfaltu niskotemperaturowego. Z.N. Budownictwo, PWN, z.113, nr 1799, s.161-168, Kraków 2008

[15] Paleczek W., Analiza doświadczalna i numeryczna uszkodzeń elementów konstrukcyjnych spowodowanych siłami statycznymi i dynamicznymi. Zeszyty Naukowe Politechniki Częstochowskiej 160, 12, Częstochowa 2005

[16] Paleczek W., Mathcad w algorytmach. Akademicka Oficyna Wydawnicza EXIT, Warszawa 2005

[17] Paleczek W., Metody analizy danych (na przykładach). Wydawnictwa Politechniki Częstochowskiej, Częstochowa 2004

[18] Paleczek W., Prognozowanie miejsca pęknięcia płyty betonowej przy wykorzystaniu numerycznej mapy wytężenia. Drogownictwo 2004, 5, 155-159

[19] Partyka J., Fizyczne podstawy procesu krzepnięcia wody w wilgotnych budowlanych materiałach porowatych. Przegląd Budowlany 9/2014, s.46-50

[20] Pentlakowa Z., WojnoT., Własności techniczne skał. Wydawnictwa Geologiczne, Warszawa 1956

[21] Pobocha M., Odporność na działanie wody i mrozu betonu asfaltowego. Z.N. Politechniki Śląskiej, z.109, nr 1735, s.301-308, 2006

[22] Pobocha M., Wpływ wypełniacza mieszanego na odporność betonu asfaltowego na oddziaływanie wody i mrozu. Z.N. Budownictwo, PWN, z.113, 1799, Kraków 2008

[23] Radziszewski P., Piłat P., Nawierzchnie asfaltowe. WKiŁ, Warszawa 2007

[24] Skalmierski B., Mechanika analityczna i teoria drgań. Wydawnictwo Politechniki Częstochowskiej, Częstochowa 2001

[25] Sybilski D. (red.), Katalog przebudów i remontów nawierzchni podatnych i półsztywnych, GDDKiA, IBDiM, Warszawa 2013

[26] Szydło A., Wpływ poziomych obciążeń na stan naprężeń wybranych typowych konstrukcji nawierzchni drogowych. Trwałe i bezpieczne nawierzchnie drogowe, Kielce 1998, 361-368

[27] Średniawa B., Hydrodynamika i teoria sprężystości. PWN, Warszawa 1977

[28] Trębacki K., Królicka A., Rozkład ciśnień hydrodynamicznych na ściankach drgających zbiorników, Bezpieczeństwo i Ekologia, 6, 2017, s.445-450

[29] Wolschin G., Hydrodynamik. Universität Heidelberg, Institut für Theoretische Physik, Heidelberg 2015

[30] Wyrwał J., Podstawy fizyczne procesu zamarzania wody w porowatych materiałach budowlanych. Politechnika Opolska, Komisja Inżynierii Budowlanej Oddział Polskiej Akademii Nauk w Katowicach, Roczniki Inżynierii Budowlanej, z. 6/2006

[31] Zienkiewicz O.C., Metoda elementów skończonych. Arkady, Warszawa 1972